Journal of Zhejiang University-SCIENCE A (Applied Physics & Engineering) 2024 25(4):292-310
www.jzus.zju.edu.cn; www.springer.com/journal/11582
E-mail: jzus_a@zju.edu.cn

Research Article

https://doi.org/10.1631/jzus.A2300243

Check for updates

# Influence of overhanging tool length and vibrator material on electromechanical impedance and amplitude prediction in ultrasonic spindle vibrator

Rendi KURNIAWAN[1], Moran XU[1], Min Ki CHOO[1], Shuo CHEN[1], Yein KWAK[1], Jielin CHEN[1], Saood ALI[1], Hanwei TENG[1], Pil Wan HAN[2]✉, Gi Soo KIM[3], Tae Jo KO[1]✉

[1]*Precision Machining Laboratory, Department of Mechanical Engineering, Yeungnam University, Gyeongsan-si, Gyeongbuk-do, Republic of Korea*
[2]*Korea Electrotechnology Research Institute (KERI), Changwon-si, Gyeongsangnam-do, Republic of Korea*
[3]*KASWIN Co., Ltd, Changwon-si, Gyeongsangnam-do, Republic of Korea*

**Abstract:** This study presents the development of an ultrasonic transducer with a radius horn for an ultrasonic milling spindle (UMS) system. The ultrasonic transducer was intended to have a working frequency of approximately 30 kHz. Two different materials were considered in the study: stainless steel (SS 316L) and titanium alloy (Ti-6Al-4V). Titanium alloy gave a higher resonance frequency (33 kHz) than stainless steel (30 kHz) under the same preload compression stress. An electromechanical impedance simulation was carried out to predict the impedance resonance frequency for both materials, and the effect of the overhanging toolbar was investigated. According to the electromechanical impedance simulation, the overhanging toolbar length affected the resonance frequency, and the error was less than 3%. Harmonic analysis confirmed that the damping ratio helps determine the resonance amplitude. Therefore, damping ratios of 0.015–0.020 and 0.005–0.020 were selected for stainless steel and titanium alloy, respectively, with an error of less than 1.5%. Experimental machining was also performed to assess the feasibility of ultrasonic-assisted milling; the result was a lesser cutting force and better surface topography of Al 6061.

**Key words:** Ultrasonic spindle; Ultrasonic vibration assisted-milling (UVAM); 1-degree of freedom (DOF); Frequency; Amplitude; Milling

## 1 Introduction

Difficult-to-machine materials, such as ceramic ($Al_2O_3$, SiC, and $ZnO_2$) (Boccaccini, 1997) or nickel-based superalloys (inconel) (Choudhury and El-Baradie, 1998), have poor machinability characteristics such as minimal thermal conductivity and extreme toughness, which produce excessive tool wear and poor smoothness. Therefore, non-traditional machining like vibration-assisted cutting is required for these materials; it enhances their machinability (Wang et al., 2014). Since the introduction of vibration-assisted cutting in the late 1950s, ultrasonic vibrators for vibration-assisted cutting methods have developed rapidly (Zheng et al., 2020) for milling (Shen et al., 2012a), turning (Amini et al., 2008), drilling (Jallageas et al., 2013), and grinding (Li et al., 2017). As an alternative cutting method for difficult materials, vibration-assisted cutting delivers low cutting energy, little heat generation, low tool-failure rate, and good surface integrity.

In vibration-assisted cutting, the ultrasonic vibrator generally follows the principle of resonance (Zheng et al., 2020), and has a rod-shaped bar with a typical piezoelectric actuator. The general ultrasonic vibrator components (e.g., piezoelectric transducer, booster, and horn) are typically used in ultrasonic welding (Kumar et al., 2017) or ultrasonic machining (USM) (Thoe et al., 1998). The piezoelectric transducer is the main source of vibration, in which the electrical excitation is converted to mechanical vibration in the longitudinal direction using the principle of self-excited

✉ Pil Wan HAN, pwhan@keri.re.kr
Tae Jo KO, tjko@yu.ac.kr
Tae Jo KO, https://orcid.org/0000-0003-1465-696X

Received May 4, 2023; Revision accepted June 5, 2023;
Crosschecked Oct. 25, 2023; Online first Dec. 12, 2023

vibration under resonance conditions. The booster and horn are used to amplify the vibration magnitude. The cutter tip is generally affixed to the end of the horn, where the magnitude is amplified. Generally, the resonance frequency for an ultrasonic vibrator is greater than 20 kHz (Kumar et al., 2017), while the oscillation magnitude is 0.1–20.0 μm (Kremer et al., 1981).

The ultrasonic vibrator was used with ultrasonic oscillation for optimal milling performance. Its design principle is the same as that of an ultrasonic vibrator in USM. Usually, it involves a milling cutter tool, ultrasonic horn, and ultrasonic transducer (Chen et al., 2018), and vibrates only in one direction (1-degree of freedom (DOF)). Ostasevicius et al. (2013) conducted vibration-assisted milling using a vibrating milling tool installed in the conventional milling spindle with a standard arbor holder (DIN 6359). Their tool vibrated in resonance mode at 14.05 and 18.40 kHz with different milling-tool-cutter lengths of 74 and 96 mm, respectively. The amplitude, based on experiments and simulation, was approximately 1 μm. Shen et al. (2012a) developed a vibrator to vibrate the workpiece instead of the milling cutter. Their vibrator operated at an ultrasonic frequency range of 19.58 kHz, and the vibrator amplitude was extremely small (~0.4 μm). Commercial rotary ultrasonic machines, such as Sonic-Mill (series 10) (Zhang et al., 2014), DMG MORI (ultrasonic 20 linear) (Marcel et al., 2014; Kuruc, 2020), and Altrasonic (Namlu et al., 2022), are already on the market.

The design-scheme analysis of 1-DOF ultrasonic transducers, for instance, the frequency analysis and harmonic response analysis (HRA), becomes a standard analysis for evaluating or predicting dynamic performance (Kandi et al., 2020; Bie et al., 2021; Chen et al., 2022). Kandi et al. (2020) invented a 1-DOF ultrasonic vibratory tool for the turning method. However, their transducer had a low resonance frequency, about 20 kHz, while the simulated amplitude was high, approximately 44 μm. Additionally, amplitude was not measured experimentally. Chen et al. (2022) developed a similar 1-DOF ultrasonic transducer for an ultrasonic welding system. The impedance frequency analysis was thoroughly carried out under different loads. Nevertheless, the resonance frequency was approximately 20 kHz, based on simulation and experimental verification. The experimental amplitude was not discussed in their report. Bie et al. (2021) proposed a 1-DOF ultrasonic transducer for ultrasonic-assisted grinding of gear systems. The resonance frequency of their apparatus was between 19 and 20 kHz and depended on the geometrical dimensions of the gears. Their experimental amplitude was around 6.70 to 6.85 μm, which is insufficient for high-speed cutting.

The finite-element (Jagadish and Ray, 2018; Kurniawan et al., 2019; Patel et al., 2021), transfer-matrix (van Kervel and Thijssen, 1983; Cornogolub et al., 2014; Wang L et al., 2018), impedance-circuit (Zhang Q et al., 2015; Yang et al., 2017; Zhang JG et al., 2019), and mechanical mass-spring-damper (MSD) (Babitsky et al., 2004; Voronina and Babitsky, 2008; Wang and Tsai, 2011) methods are commonly used to determine the resonance frequency in ultrasonic transducer development. The transfer-matrix and MSD methods require advanced analysis. It is not easy to evaluate the resonance frequency if the geometry becomes complex. The finite-element method (FEM) can overcome this problem because of its suitability for complex transducer geometry. Resonance frequency can be obtained accurately by modal simulation and the harmonic-response method. However, electrical energy loss and temperature effect of the ultrasonic transducer are still major challenges in FEM. Patel et al. (2021) developed an ultrasonic horn based on FEM analysis of the modal and harmonic simulation. Their hybrid horn performed better than others. Amplitude (directional deformation) and stress (von-Mises) are major output interests in FEM. Meanwhile, impedance-circuit analysis has been utilized for ultrasonic transducers in many ways since Mason's equivalent circuit (Bybi et al., 2019) was discovered. Zhang et al. (2015) derived an electromechanical impedance model for a longitudinal ultrasonic transducer by considering the influence of piezoelectric ceramic positioning and the effective electromechanical coupling coefficient. Zhang et al. (2019) also derived an electromechanical impedance model by considering the effect of tightening torques. While the electromechanical impedance has been derived, the effect of the overhanging length (OL) and different materials has not yet been investigated.

One-directional (1-DOF) and two-directional vibration (2-DOF) resonance transducers have been developed for milling/drilling/grinding. Geng et al. (2014, 2015) cut the carbon-fiber-reinforced-plastic (CFRP) using a resonance transducer, which vibrated elliptically in rotary ultrasonic machine (RUM). Two groups

of piezo transducers (PZTs) were used. The front cylinder was titanium alloy and the back cylinder was stainless steel. The coupling effect was created between two bending-vibration modes. The group's transducer vibrated at 20.6 kHz with two similar bending amplitudes of approximately 5 μm. Han and Zhang (2020) conducted experiments on a resonance vibrator with a similar frequency but higher amplitude than Zhang et al. (2020)'s resonance vibrator. Liu et al. (2023) recently developed a 2-DOF resonance transducer for application in ultrasonic peening drilling. Their resonance frequency was 21.38 kHz and their amplitude was 5 μm. Moreover, resonance devices using the coupling effect between two vibration modes have also been developed (for example between the longitudinal and torsional modes). In general, the longitudinal vibration mode is paired with the torsional vibration mode with the help of a groove slot on the horn surface (Wu et al., 2019; Chen et al., 2021). A similar concept of implementing the groove slot on the horn surface is found in a few other researchers' designs (Liu et al., 2017; Wang JJ et al., 2018; Zhao et al., 2019; Pang et al., 2020, 2021; Li et al., 2021).

In addition to the 2-DOF design, a 3-DOF resonance-transducer design for milling has been reported (Gao and Altintas, 2019). The University of British Columbia developed a 3-DOF resonance transducer for milling or drilling (Gao and Altintas, 2019). This resonance vibrator fundamentally uses the principle of resonance coupling between longitudinal and two-bending modes. The resonance-vibrator frequency was roughly 17 kHz. However, the vibration amplitude was high: 20–25 μm. Kurniawan et al. (2021) developed a 3-motion resonance vibrator which was not used for milling. Instead, it was perfect for micro-grooving. The structure of their vibrator, which uses a prismatic or triangle pyramid horn, might not be suitable for rotational operation because perfect balance during rotation is not guaranteed. The working frequency was adequate at ~24 kHz, but the vibration amplitude was very small at 0.4–0.6 μm. Shamoto et al. (2005) developed a 3-DOF resonance vibrator for surface sculpturing in milling. Their vibrator used asymmetrical locations for the PZT plates due to balancing problem; it might be suitable only for low rotational speeds.

Although 1-, 2-, and 3-DOF resonance vibrators already exist for milling or drilling, or even for grinding, we were still interested in developing a 1-DOF resonance vibrator. This study focuses on impedance frequency and amplitude prediction, taking into consideration the effect of the OL and the different materials used for parts. In amplitude prediction, damping-ratio determination is still rarely carried out. Therefore, the objective of this paper is to propose an impedance and damping-ratio model to predict resonance frequency and vibration amplitude, which incorporates the effect of OL and different materials for a 1-DOF resonance vibrator in milling-drilling operation.

## 2 1-DOF ultrasonic resonance transducer design

Fig. 1 shows a typical design for a 1-DOF ultrasonic resonance transducer. It generally consists of a horn and transducer (Thoe et al., 1998). In this study, however, to decrease the amount of material and the mass, we simplified Zhang et al. (2019)'s transducer design. The toolbar behaves like an extension of the horn, which has a relationship to the resonance frequency. The device consisted of a back mass, radius horn with flange, nut and collet, toolbar, and four PZT-4 sets.

Modal simulation was carried out in ANSYS Academic version 19.2 to analyze the resonance frequency during the process design. The fixed boundary condition had been given on the flange surface. The boundary condition used in the modal analysis was similar to the HRA. Table 1 inventories the physical properties used to conduct modal analysis. In the process design, the resonance frequency was set to 30 kHz when the toolbar was uninstalled. However, the 1st mode decreased to approximately 20 kHz due to the added mass of the steel toolbar. The effect of the toolbar must be considered because it is used for milling/drilling. Fig. 2 and Table 2 show the outcomes of the modal simulation in ANSYS with a transducer made from different materials. We found that if the device works based on the 1st longitudinal mode (Fig. 1b), the resonance frequency is very low (lower than 25 kHz). If the device works based on the 2nd longitudinal mode (Fig. 1c), the frequency is more than 25 kHz.

The OL of the toolbar affects the resonance frequency of the transducer (Fig. 2), which decreases when the toolbar length increases. In this study, we investigated two materials, titanium alloy (Ti-6Al-4V) and

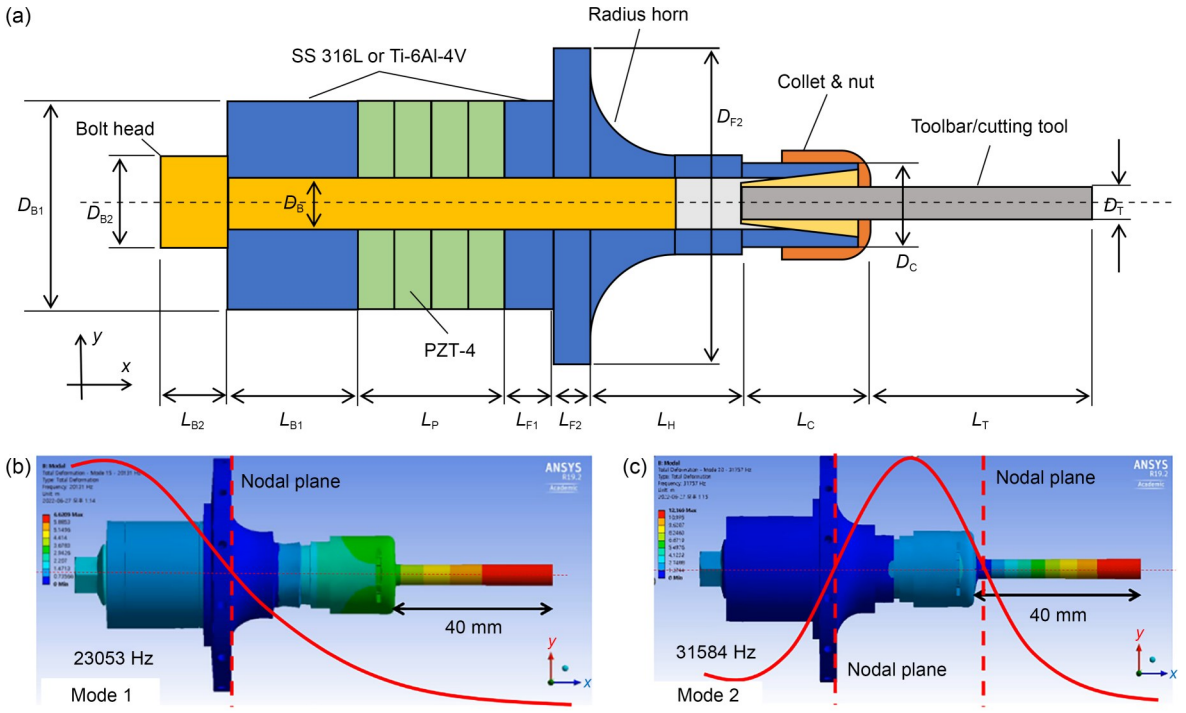


**Fig. 1 Design of a 1-DOF ultrasonic resonance transducer made of SS 316L or Ti-6Al-4V: (a) schematic diagram; (b) 1st longitudinal mode; (c) 2nd longitudinal mode. *L*: length; *D*: diameter. Subscripts: B: screw bolt; P: piezoelectric ceramic actuator; T: toolbar; F: front mass; H: horn; C: collet & nut**

**Table 1 Material properties of the 1-DOF component for modal and harmonic analysis**

| Part | Material | Mass density, $\rho$ (kg/m$^3$) | Young's modulus, $E$ (N/m$^2$) | Poisson's ratio, $v$ |
|---|---|---|---|---|
| Radius horn/back mass (ANSYS database) | SS 316L | 8027 | $2.00\times10^{11}$ | 0.265 |
| | Ti-6Al-4V | 4430 | $1.05\times10^{11}$ | 0.310 |
| Toolbar/screw bolt (ANSYS database) | Structural steel | 7850 | $2.00\times10^{11}$ | 0.300 |
| Piezoelectric actuators (Deangelis and Schulze, 2016) | PZT-4 | 7650 | $5.89\times10^{10}$ | 0.310 |

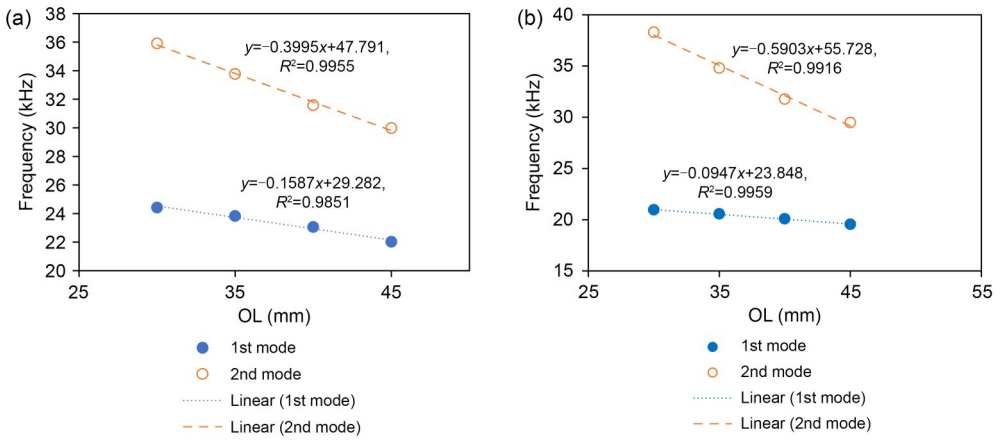


**Fig. 2 Modal analysis frequency for the 1st and 2nd modes with SS 316L (a) and Ti-6Al-4V (b)**

stainless steel (SS 316L), to determine which would perform better. It can be seen from Table 2 that titanium alloy gave a higher resonance frequency than stainless steel.

**Table 2 Modal results corresponding to Fig. 2**

| OL (mm) | Frequency (Hz) | | | |
|---|---|---|---|---|
| | Stainless steel (SS 316L) | | Titanium alloy (Ti-6Al-4V) | |
| | 1st mode | 2nd mode | 1st mode | 2nd mode |
| 30 | 24.416 | 35.909 | 20.972 | 38.308 |
| 35 | 23.828 | 33.764 | 20.571 | 34.805 |
| 40 | 23.053 | 31.584 | 20.090 | 31.774 |
| 45 | 22.030 | 29.977 | 19.554 | 29.480 |

## 3 Harmonic response analysis

The amplitude output on the tip of the rod bar was predicted by carrying out HRA (Namlu et al., 2022) during excitation by different voltages. The HRA was performed using the Academic version 19.2 of ANSYS. HRA can produce a frequency response function (FRF) graph, which allows frequency and amplitude to be investigated. In this analysis, however, the amplitude becomes a major concern. Nevertheless, the peak frequency is not a concern because the value is close to that in the experiment described in Section 6.2.

Fig. 3 shows the boundary conditions for the HRA using PZT add-ins. The material properties in the HRA are similar within those in the modal analysis (Table 1). The PZT add-ins (application customization toolkit (ACT) piezo and MEMS version 190.1) was installed to give boundary conditions to the piezoelectric body. We chose a 40-mm OL rod bar because the maximum resonance amplitude was measured within 40–43 mm (Section 6.2). We chose ANSYS standard meshing with an element number of 12422 and node number of 27766, taking into consideration the fact that the Academic version 19.2 has limitations with regard to generating detailed meshing. A fixed constraint on the flange surface was given, because the experiment was clamped in the spindle structure. The piezoelectric body of PZT-4 was chosen for 4-piezo. The charge constant, compliance, elastic, and strain (Othmani et al., 2020) for PZT-4 are given in Section S1 of the electronic supplementary materials (ESM). The output of the harmonic response was set on the tip of the rod bar, as shown in Fig. 3.

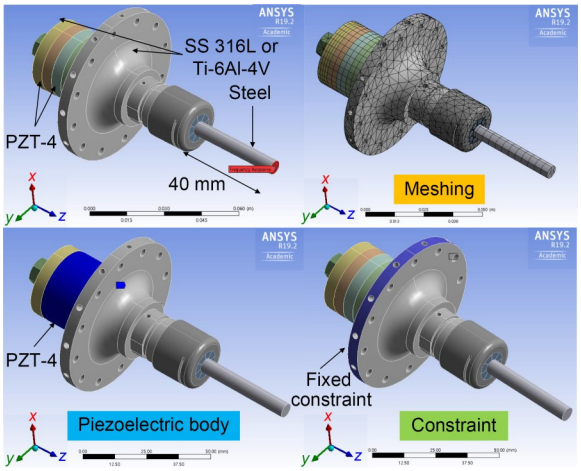


**Fig. 3 Boundary conditions for the HRA using PZT add-ins**

## 4 Electromechanical impedance modeling

The electromechanical impedance method was adopted to predict the resonance frequency from the impedance resonance frequency because it gives an effective solution (McBrearty et al., 1988). We adopted Zhang et al. (2019)'s impedance model of an ultrasonic transducer with slight modifications to the transducer structure, shape, and configuration. Each component for the electromechanical impedance method could be described as a T-shaped impedance structure.

### 4.1 Electromechanical impedance of PZT

In the case of a piezo material, the impedance circuit is in series with an electromechanical transformer because the secondary winding is coupled with the primary winding by static capacitance $C_o$, voltage input $V_i$, and current $I$, as shown in Fig. 4. The static capacitance value of the piezoelectric ceramic $C_o$ (Al Ahmad and Plana, 2009) is described by Eq. (1).

$$C_o = n_p \cdot \varepsilon_{33}^T \cdot \frac{A_o}{L_o}, \tag{1}$$

where $n_p$ is equal to the number of piezoelectric ceramic actuators installed; $\varepsilon_{33}^T$ is equivalent to the permittivity; $A_o$ is the cross-section area of PZT, which is equivalent to $A_o = \frac{1}{4}\pi(D_o^2 - D_i^2)$. $D_o$ is the PZT outer diameter and $D_i$ is the PZT inner diameter. $L_o$ is the PZT thickness. The electromechanical conversion coefficient $N$ can be expressed as in Eq. (2) (Li et al., 2022).

$$N = n_p \cdot \frac{d_{33}}{S_{33}^E} \cdot \frac{A_o}{L_P}, \tag{2}$$

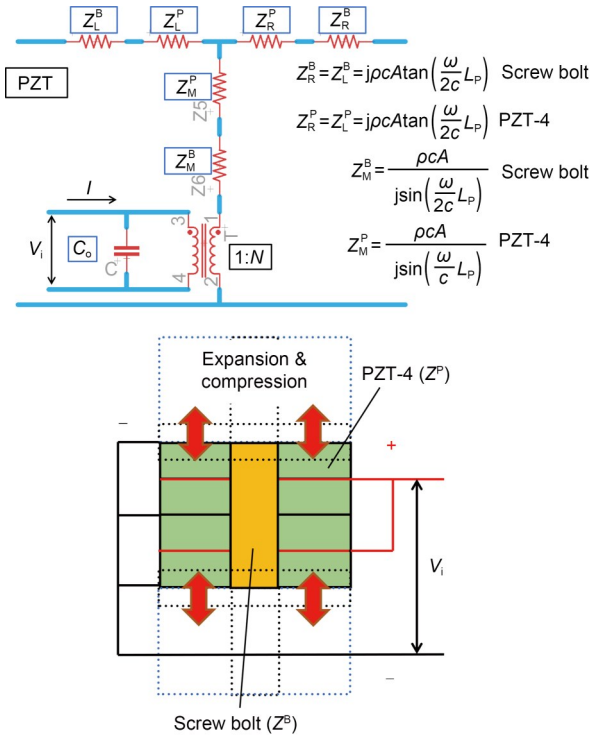


**Fig. 4 Equivalent impedance circuit for the piezoceramic stack and screw bolt. *N*: piezoelectric coupling factor (electromechanical conversion coefficient); *Z*: impedance factor, with a T-shaped impedance configuration. Subscripts: L indicates left, R indicates right, and M indicates middle**

where $d_{33}$ is equal to the PZT charge constant; $S_{33}^{E}$ is equal to the PZT elastic compliance; $n_p$ is equal to the number of PZT stacks; $L_P$ is equal to the total length of the PZT stack.

Thus, the equivalent impedance circuit (Eqs. (3)–(6)) for piezoceramic ceramic stacks, including the screw bolt, is shown in Fig. 4 (Lin et al., 2018). j is the complex number.

$$Z_R^B = Z_L^B = jZ_0^B \tan\left(\frac{\tau^B \cdot n_p \cdot L_o}{2}\right), \tag{3}$$

$$Z_R^P = Z_L^P = jZ_0^P \tan\left(\frac{\tau^P \cdot n_p \cdot L_o}{2}\right), \tag{4}$$

$$Z_M^B = \frac{Z_0^B}{j\sin\left(\tau^B \cdot n_p \cdot L_o\right)}, \tag{5}$$

$$Z_M^P = \frac{Z_0^P}{j\sin\left(\tau^P \cdot n_p \cdot L_o\right)}, \tag{6}$$

where the specific acoustic impedances $Z_0^B$ and $Z_0^P$ are the multiplications of the density $\rho$ with the acoustic velocity of the material $c=\sqrt{E/\rho}$ and the total cross-section area $A$ between a screw bolt and PZT, respectively. Thus, the specific acoustic impedance $Z_0^i$ can also be described by Eq. (7), where the superscript $i$ is either for B or P.

$$Z_0^i = \rho \cdot c \cdot A. \tag{7}$$

The material propagation constant $\tau^i$ can be described by Eq. (8), where the superscript $i$ is either for B or P; $\omega=2\pi f$, and $f$ is the frequency based on the sampling data from 16 to 50 kHz for the frequency-response function.

$$\tau^i = \frac{\omega}{c}. \tag{8}$$

### 4.2 Electromechanical impedance transducer

Fig. 5 illustrates that each component of the electromechanical impedance can be described as a T-shaped impedance structure. Here, $Z_L$ denotes the total corresponding impedance for the PZT left-side region, as described by Eq. (9); $Z_R$ denotes the total corresponding impedance for the PZT right-side region, as described by Eq. (10). For the left side, it consists of the left impedance of PZT ($Z_L^P$), the left impedance of the screw bolt ($Z_L^B$), and the equivalent impedance of the back mass ($Z_L^{BM}$), which is described in Section S1 of the ESM; for the right side, it consists of the right impedance of PZT ($Z_R^P$), the right impedance of the screw bolt ($Z_R^B$), and the total corresponding impedance of the radius horn, nut and collet, and cutting tool ($Z_{F1}$). $Z_{F1}$ is described in Section S1 of the ESM.

$$Z_L = Z_L^P + Z_L^B + Z_L^{BM}, \tag{9}$$

$$Z_R = Z_R^P + Z_R^B + Z_{F1}. \tag{10}$$

Therefore, the total mechanical impedance $Z_m$ is expressed by Eq. (11).

$$Z_m = Z_M^B + Z_M^P + \left\{\frac{Z_R \times Z_L}{Z_R + Z_L}\right\}, \tag{11}$$

where $Z_M^B$ is determined by Eq. (5), $Z_M^P$ is determined by Eq. (6), $Z_L$ is determined by Eq. (9), and $Z_R$ is determined by Eq. (10). Then, the electromechanical corresponding impedance $Z_e$ can be expressed by Eq. (12) (Zhang et al., 2019).

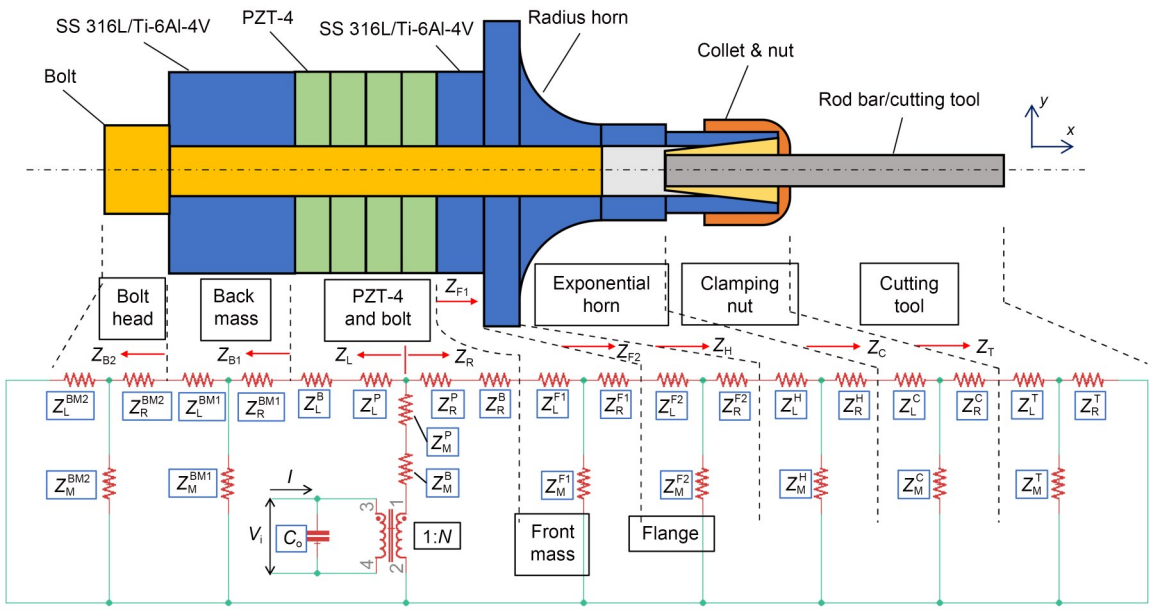


**Fig. 5 Equivalent circuit model with T-type equivalent impedance structure**

$$Z_e = \frac{Z_{C_o} \times N^2 \cdot Z_m}{Z_{C_o} + N^2 \cdot Z_m}, \tag{12}$$

where $Z_{C_o}$ is the impedance of the capacitance, which is expressed by Eq. (13). $N$ is determined by Eq. (2), and $Z_m$ by Eq. (11).

$$Z_{C_o} = \frac{1}{j\omega C_o}, \tag{13}$$

where $\omega$ is the angular frequency ($\omega=2\pi f$) and $C_o$ is determined by Eq. (1).

### 4.3 Electromechanical impedance of the solid structure

Our ultrasonic transducer consisted of solid structures, including the radius horn, back mass, collet and nut, toolbar, and screw bolt. The back mass, toolbar, and screw bolt had a solid structure and a cylindrical shape. Table S1 in the ESM lists the typical acoustic impedance equation for the T-shape impedance structure for the exponential and cylindrical shapes.

In the case of the radius horn, we simplified its profile from a radius shape to an exponential shape. As shown in Fig. 6a, the real shape of the radius horn was close enough to the exponential equation, which represents the exponential horn. Based on the data graphed in Fig. 6a, the exponential equation is $y=7.107e^{-0.4999x}$.

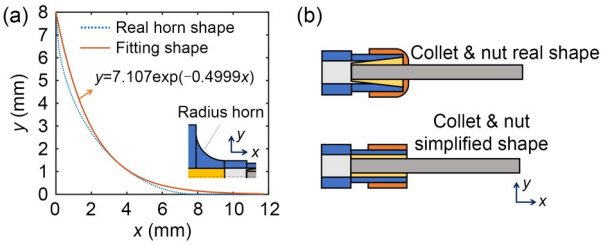


**Fig. 6 Simplification of the horn profile (a) and nut clamping (b)**

The nut and collet structure was hard to analyze. Without losing the original shape, the simplification for nut-clamping was made, as shown in Fig. 6b. The shapes of all the nuts and collets were simplified to be cylindrical. Therefore, we used the acoustic impedance equation in Table S1 of the ESM for the simulation. Table 3 lists the material properties and dimensions used for the electromechanical impedance modeling. Typically, the properties of stainless steel are similar to those of common steel (Zhang et al., 2019). The simulated impedance result is described in detail in Section 6.

## 5 Experimental setup

### 5.1 Experimental impedance setup

The preload compression stress was applied with a torque wrench, and the compression stress was measured using a piezo clamping device, which was

**Table 3 Material properties used in the electromechanical impedance modeling**

| Material | Density (kg/m$^3$) | Poisson's ratio | Property |
|---|---|---|---|
| PZT-4 (Zhang et al., 2019) | 7700 | 0.25 | $d_{33}$=270(1–0.0003j) pC/N, $S_{33}^{E}$=2×10$^{11}$(1–0.0012j) m$^2$/N, $\varepsilon_{33}^{T}=1300\times\varepsilon_0$, $\varepsilon_0=8.8452\times10^{-12}$ F/m |
| Screw bolt (steel) (Zhang et al., 2019) | 8000 | 0.28 | $E$=2.00×10$^{11}$(1+0.001j) N/m$^2$ |
| Screw bolt (Ti-6Al-4V) | 4430 | 0.31 | $E$=1.05×10$^{11}$(1+0.001j) N/m$^2$ |
| Back mass (steel) (Zhang et al., 2019) | 8000 | 0.28 | $E$=2.00×10$^{11}$(1+0.001j) N/m$^2$ |
| Back mass (Ti-6Al-4V) | 4430 | 0.31 | $E$=1.05×10$^{11}$(1+0.001j) N/m$^2$ |
| Front mass & flange (steel) (Zhang et al., 2019) | 8000 | 0.28 | $E$=2.00×10$^{11}$(1+0.001j) N/m$^2$ |
| Front mass & flange (Ti-6Al-4V) | 4430 | 0.31 | $E$=1.05×10$^{11}$(1+0.001j) N/m$^2$ |
| Horn (steel) (Zhang et al., 2019) | 8000 | 0.28 | $E$=2.00×10$^{11}$(1+0.001j) N/m$^2$ |
| Horn (Ti-6Al-4V) | 4430 | 0.31 | $E$=1.05×10$^{11}$(1+0.001j) N/m$^2$ |
| Clamping nut (steel) (Zhang et al., 2019) | 8000 | 0.28 | $E$=2.00×10$^{11}$(1+0.001j) N/m$^2$ |
| Cutting tool (HSS) (Noda et al., 2017) | 7600 | 0.28 | $E$=2.33×10$^{11}$(1+0.01j) N/m$^2$ |

HSS: high-speed steel; $\varepsilon_0$: permittivity constant

targeted to a specific value (e.g., 2 MPa). The preload compression stress ranged from 2 to 20 MPa. We tested the free condition (unclamped) and the clamped condition on the jig to determine whether there was a significant frequency change. For the unclamped condition, the ultrasonic transducer was placed on soft foam. We utilized an impedance analyzer (type PV520A) made by Hangzhou Precision Machinery Co. Ltd., China to check the FRF impedance of the ultrasonic transducer with different preload compression-stress levels. We also investigated the effect of the OL of the toolbar. The mass of the toolbar rod was approximately 13.32 g, with a maximum length of 60 mm; the rod-bar material was HSS.

## 5.2 Experimental amplitude setup

Fig. 7 presents the experimental amplitude setup for the ultrasonic transducer, in which an overhanging toolbar was installed. The excitation voltage was generated using a USG-2A ultrasonic generator (Hybrid Precision Corp., Republic of Korea). The generator gave an input voltage in a square waveform, and peak-to-peak voltages of 100, 200, and 300 V were generated. We used a data-acquisition (DAQ) type USB-6363 created by National Instruments (NI), USA to record the amplitude from the optical fiber sensor amplifier. The optical fiber sensor was placed on the tip of the tool rod bar, and the OL effect was evaluated. The effect of the overhanging tool rod bar was analyzed by specifying a length of 30–50 mm with the total rod bar length of 60 mm.

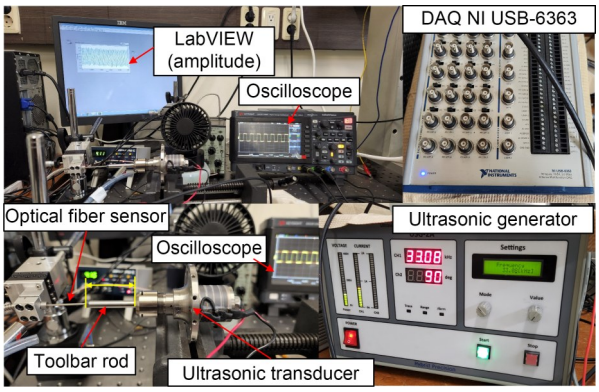


**Fig. 7 Experimental setup for amplitude measurement**

## 5.3 Experimental milling setup

Fig. 8 shows the experimental ultrasonic vibration-assisted milling (UVAM) setup with an ultrasonic transducer of titanium alloy (Ti-6Al-4V), selected due to its superior vibration characteristics. A machining experiment on a ductile material such as aluminum alloy (Al 6061), was essential for examining the feasibility of the ultrasonic transducer. The force was captured using a dynamometer KISTLER type 9257 A, and the DAQ 6363 was used to record force fluctuation after amplification. The trials were carried out three times for each parameter. The three-phase inverter generated an excitation voltage to rotate the induction motor for the built-in spindle motor. We used the USG-2A ultrasonic generator, and the ultrasonic input voltage was approximately 100 V. Constant amplitude and ultrasonic frequency were maintained. The machined surface

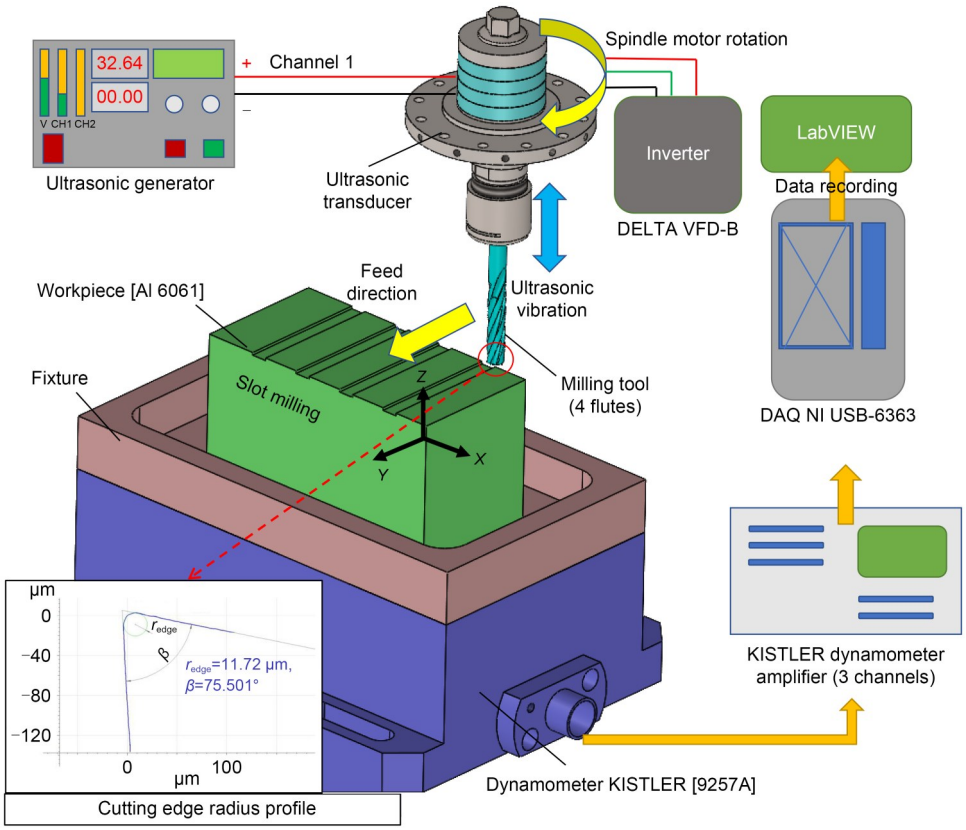


**Fig. 8 UVAM cutting diagram and experimental cutting setup**

roughness after slot milling was quantified using a Mitutoyo roughness tester (SJ-310). We also assessed the 3D surface profile using a Nanosystem 3D surface measurement system (NV-2000).

Table 4 lists the UVAM parameters used to test the feasibility of the ultrasonic transducer. The test was conducted for a slot-milling case at three feed rates (50, 100, and 150 mm/min). The spindle rotation was set at about 3000 r/min. We applied HSS conventional end milling with four flutes made by the YG-1 tool company (E2412906K). The end-mill diameter size was 6 mm. The measured tool-edge radius $r_{edge}$ was approximately 11.72 μm and was examined using an Alicona EdgeMaster (Fig. 8). The end-milling mass was approximately 11.76 g owing to the milling-tool shape geometry, which may have affected the vibration frequency due to the mass effect, which was lower than that of the HSS tester rod bar (13.32 g). Therefore, when HSS end milling was used, the ultrasonic frequency was approximately 32.64 kHz, and the amplitude was approximately 14.2 μm. The frequency and amplitude were slightly higher than those when the HSS tester rod bar with an OL of 37 mm was used. The ultrasonic

**Table 4 Experimental UVAM setup**

| Parameter | Value | |
|---|---|---|
| | CM | UVAM |
| Rotational speed (r/min) | 3000 | 3000 |
| Cutting speed (m/min) | 56.52 | 56.52 |
| Feed rate (mm/mm) | 50, 100, 150 | 50, 100, 150 |
| Axial depth of cut (mm) | 0.5 | 0.5 |
| Radial depth of cut (mm) | 6 | 6 |
| Ultrasonic frequency (kHz) | – | 32.64 |
| Vibration amplitude (μm) | – | 14.2 |
| Workpiece material | Aluminum alloy (Al 6061) | Aluminum alloy (Al 6061) |
| Cooling condition | Dry (without coolant) | Dry (without coolant) |
| End-milling tool | HSS; four flutes; $D$: 6 mm; no coating; $r_{edge}$: 11.72 μm; mass: 11.76 g | HSS; four flutes; $D$: 6 mm; no coating; $r_{edge}$: 11.72 μm; mass: 11.76 g |

CM: conventional-milling

frequency was approximately 32.54 kHz, and the amplitude was approximately 13.47 μm (transducer material: titanium alloy; input voltage: 100 V) when the HSS tester rod bar was used (Fig. 13). We chose an overhang of 37 mm to decrease the effect of chatter vibration (Xia et al., 2020).

## 6 Results and discussion

### 6.1 Impedance results

Fig. 9 shows the typical FRF impedance of the ultrasonic transducer with a maximum compression stress of 20 MPa. The impedance FRF was swept from 16 to 40 kHz. A similar pattern of a typical FRF impedance can be found elsewhere (Milewski et al., 2015; Pérez-Sánchez et al., 2020). Fig. 9 shows the differences in the impedance FRF between unclamped and clamped for both stainless steel (Figs. 9a and 9b) and titanium alloy (Figs. 9c and 9d). In Fig. 9, the red line symbolizes the impedance magnitude, and the blue line represents the phase shift. In the FRF impedance, the higher and lower magnitudes indicate the anti-resonance and resonance frequencies, respectively. It is clear that for both materials, the frequencies become slightly higher when the ultrasonic transducer is clamped. These results indicate that the vibration characteristics improve due to higher rigidity/stiffness during clamping. On the other hand, there is a slight noise occurrence (tiny ripple) when it is clamped. The reason might be that the traveled acoustic vibration is a bit disturbed, but it not substantially. Therefore, the nodal point of the ultrasonic transducer is located near the flange.

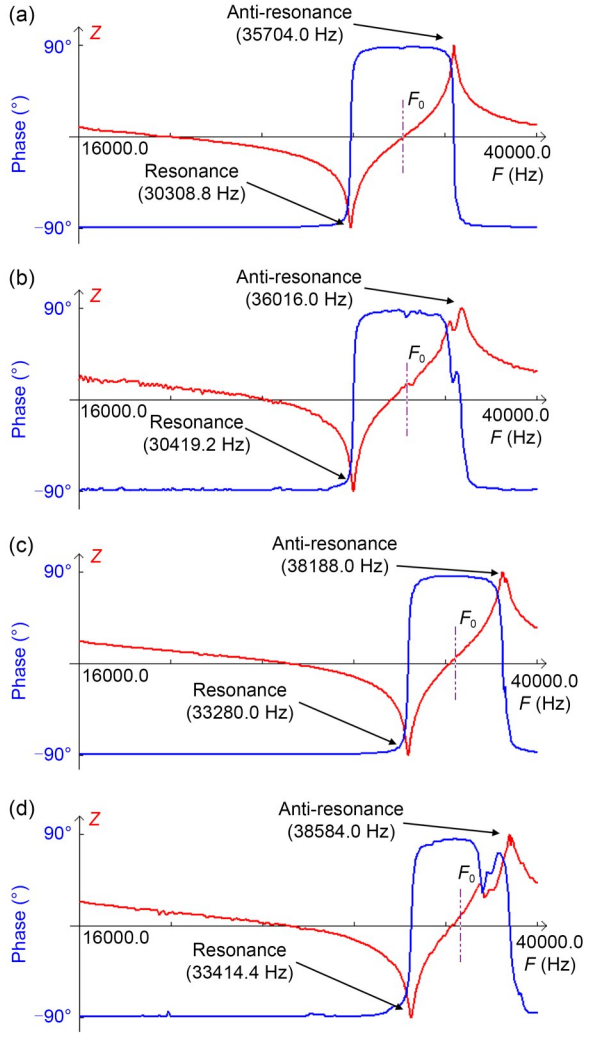


**Fig. 9 Typical unclamped (a and c) and clamped (b and d) FRF impedance *Z* of ultrasonic transducer for stainless steel (a and b) and titanium alloy (c and d) under a preload stress of 20 MPa. $F_0$ is the average frequency value between resonance and anti-resonance frequencies. References to color refer to the online version of this figure**

Fig. 10 presents the results for preload compression stress vs. frequency. If an insufficient preload is

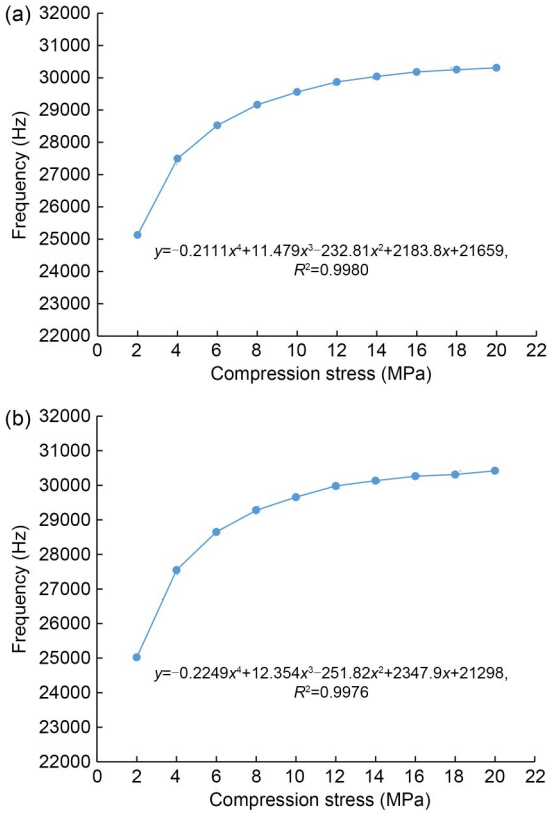


**Fig. 10 Compression preload stress vs. frequency of the ultrasonic transducer (stainless steel): (a) unclamped; (b) clamped**

applied, the frequency will be low, and the amplitude will be insufficient because the piezoelectric ceramic oscillates freely between solid bodies. On the other hand, if excessive prestress is applied, piezoceramic fracture might occur and the bolt becomes twisted during assembly (DeAngelis et al., 2015). A sufficient preload stress is required during assembly. Thus, the pattern in Fig. 10 shows that the frequency remains relatively constant if sufficient preload has been obtained. In this study, 20 MPa was an effective preload compression stress. According to DeAngelis et al. (2015), the sufficient compression stress of a Langevin transducer is between 30 and 60 MPa. Nevertheless, we found that the effective compression stress was lower than the recommended value and depended on the PZT type, material friction, thread engagement, bolt, and horn material. In addition, the difference in resonance frequency between the unclamped and clamped conditions was not notable in terms of pattern curve with variation of the preload compression stress (Fig. 10). However, as discussed above, the resonance frequency in the clamped state was slightly higher than that in the unclamped state due to a slight increase in rigidity/stiffness when it was clamped. Table 5 lists the final resonance frequency results of 20 MPa for stainless steel and titanium alloy transducer materials. Titanium alloy material had a higher frequency.

**Table 5 Resonance frequencies under a final compression preload stress of 20 MPa**

| Preload stress (MPa) | Resonance frequency (Hz) | | | |
|---|---|---|---|---|
| | Stainless steel | | Titanium alloy | |
| | Unclamped | Clamped | Unclamped | Clamped |
| 20 | 30308.8 | 30419.2 | 33280.0 | 33414.4 |

Fig. 11 compares the simulated and experimental FRF impedance values for stainless steel and titanium, with the effect of an overhanging toolbar length between 40 and 50 mm. Table 6 lists the final summary impedance resonance frequencies for the simulation and experiment. One can see from Figs. 11 and 12 that the simulated FRF values for stainless steel and titanium alloy correspond well with those in the experiment.

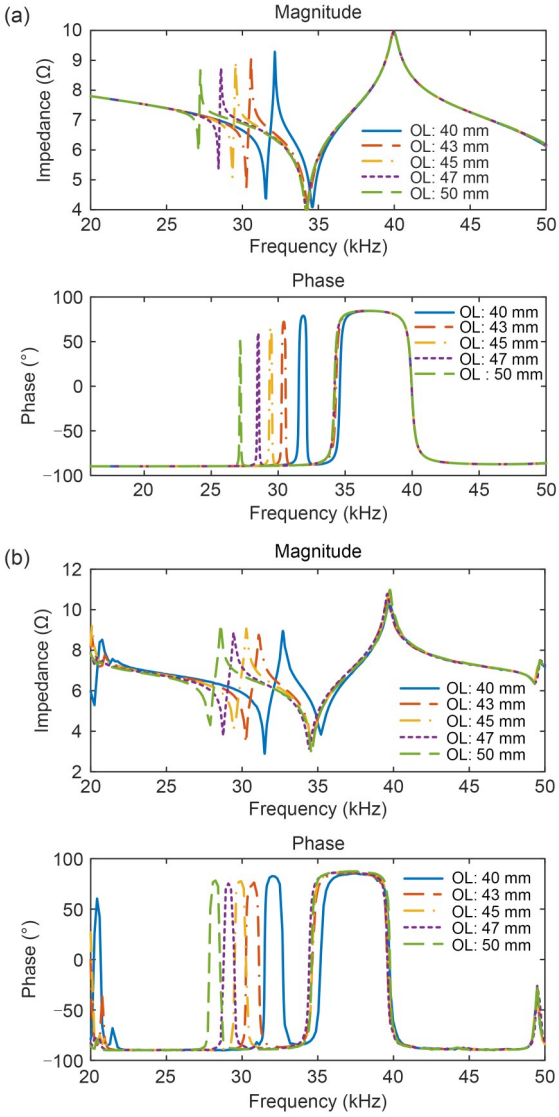


**Fig. 11 Comparison between simulated and experimental FRF impedance of an ultrasonic transducer (stainless steel) (OL: 40–50 mm): (a) simulation; (b) experiment**

**Table 6 Simulated and experimental impedance resonance frequencies of the ultrasonic transducer**

| OL (mm) | Stainless steel | | | Titanium alloy | | |
|---|---|---|---|---|---|---|
| | Simulated frequency (kHz) | Experimental frequency (kHz) | Error (%) | Simulated frequency (kHz) | Experimental frequency (kHz) | Error (%) |
| 40 | 31.519 | 31.483 | 0.11 | 32.300 | 32.320 | 0.06 |
| 43 | 30.260 | 30.259 | 0.003 | 30.770 | 30.620 | 0.48 |
| 45 | 29.341 | 29.430 | 0.30 | 29.750 | 29.600 | 0.51 |
| 47 | 28.422 | 28.750 | 1.14 | 28.790 | 28.750 | 0.14 |
| 50 | 27.095 | 27.900 | 2.89 | 27.400 | 27.390 | 0.04 |

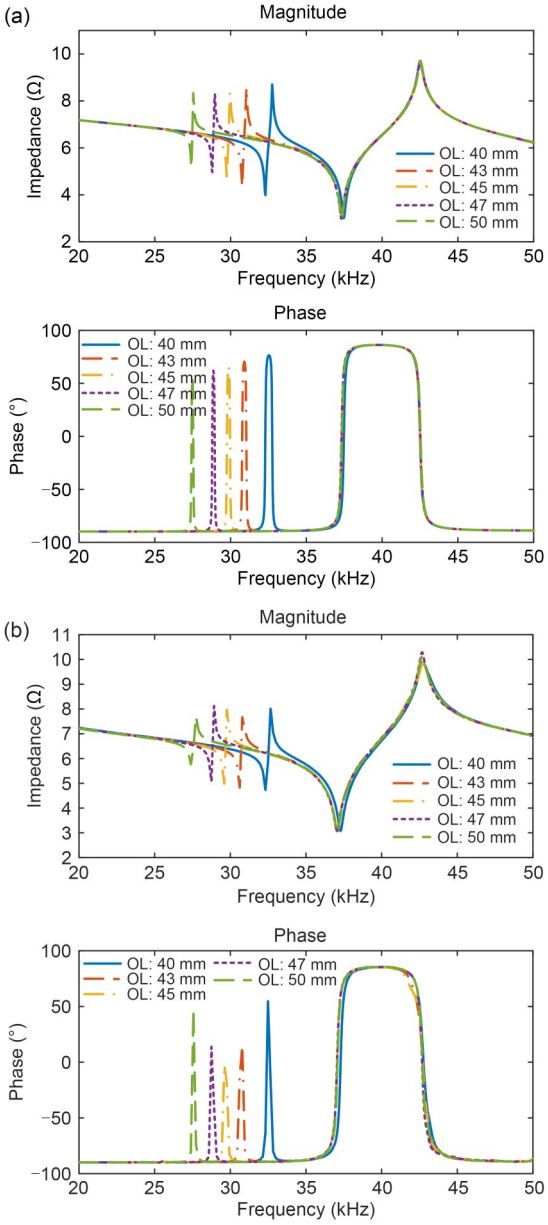


**Fig. 12 Comparison between simulated and experimental FRF impedance of an ultrasonic transducer (titanium alloy) (OL: 40–50 mm): (a) simulation; (b) experiment**

There are two peaks for each FRF impedance. The first resonance occurred because of the OL. As the OL increased, the first resonance moved to the left and the frequency became lower, which indicates that the OL increases the half acoustic wavelength $\left(L=\frac{\lambda}{2}=\frac{c}{2f}\right)$ (Pérez-Sánchez et al., 2020). Hence, the frequency decreased from 31.5 to 27.0 kHz for stainless steel and from 32.0 to 27.0 kHz for titanium alloy. In addition, the secondary frequency for titanium alloy was significantly higher than that for stainless steel, as shown in Figs. 11 and 12. Table 6 shows that the discrepancy between the simulation and experiment was small (~3%). These results indicate that the impedance simulation model can predict the resonance frequency of the ultrasonic transducer. However, the model does not consider the effect of the cutting load during machining, and the resonance frequency might differ with a cutting load. The model can therefore be improved by incorporating this factor.

### 6.2 Amplitude measurement and harmonic amplitude prediction results

The measured amplitude shows an interesting pattern for both stainless steel (Fig. 13a) and titanium alloy (Fig. 13b), with an OL between 30 and 50 mm. We investigated the effects of input voltages (100, 200, and 300 V). Fig. 13c shows the typical measured amplitude with different input voltages and an OL of 40 mm, for stainless steel. The measured amplitude was stable in the sinusoidal form, with no coupling vibration effect. Figs. 13a and 13b show that the amplitude rose and fell when the OL increased. In addition, the amplitude rose as the given voltage increased. A maximum amplitude of approximately 24.0 μm was obtained for stainless steel and of approximately 25.6 μm for titanium alloy. Hence, titanium alloy has better acoustic characteristics.

Fig. 14 shows the FRF simulated harmonic response of an ultrasonic transducer with different damping ratios and input voltages (100 and 300 V). The damping ratio $\zeta$ is an essential factor for establishing the accuracy of amplitude prediction. In the simulation, a damping ratio between 0.0025 and 0.0200 was selected for mapping the amplitude prediction. The amplitude decreased when the damping ratio value increased, as shown in Fig. 14. At the lowest damping ratio of 0.0025 (at 100 V), the input had a magnitude value of roughly 50 μm in favor of stainless steel and 30 μm in favor of titanium alloy. It was impossible to obtain a high amplitude in real situations, for instance, 30 or 50 μm, even with a low input voltage. In addition, with a high given voltage (300 V), the resonance amplitude was extremely high at approximately 100 μm in favor of titanium alloy. Therefore, we produced a mapping graph to determine the damping ratio value. Fig. 15 shows the power mode of the fitting curve of simulation results for different voltages and materials.

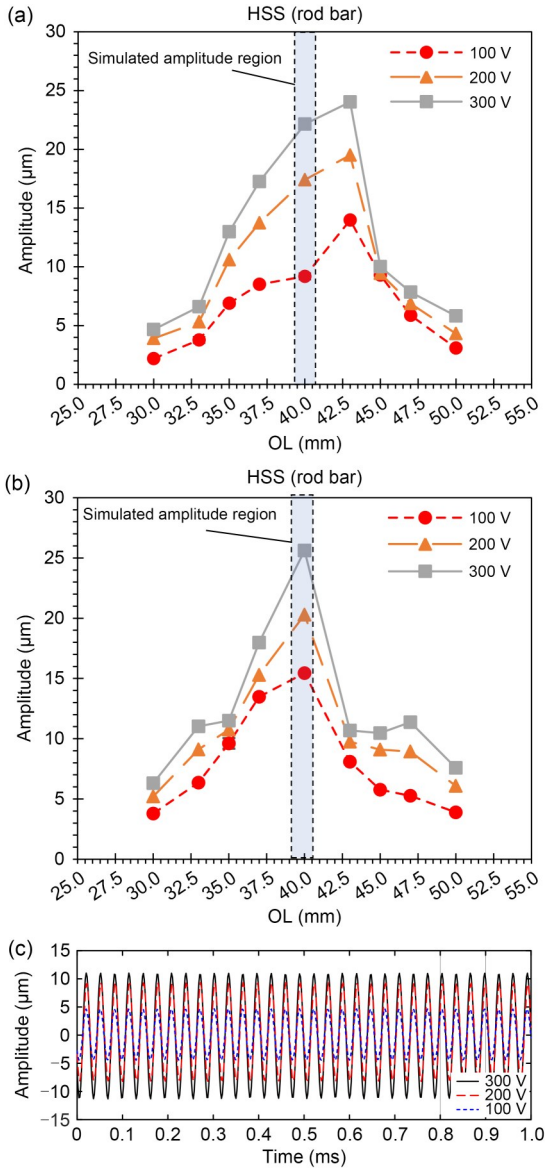


**Fig. 13 Amplitude measurement of an ultrasonic transducer with respect to the OL at different voltage inputs: (a) stainless steel; (b) titanium alloy; (c) typical amplitude with an OL of 40 mm for stainless steel**

The relationship between amplitude and damping ratio can be expressed by the equation term of $y=\alpha\zeta^{-\beta}$. $\alpha$ and $\beta$ are coefficients; $y$ is the amplitude; $\zeta$ is the damping ratio. The damping ratio must be estimated using the experimental amplitude, and it must be calibrated according to the equation in Fig. 15.

We compared the simulated amplitude prediction with the experimental results for stainless-steel and titanium-alloy transducer materials (Table 7). When a constant damping ratio was used (e.g., 0.0200 for stainless steel and 0.0100 for titanium alloy), the simulated

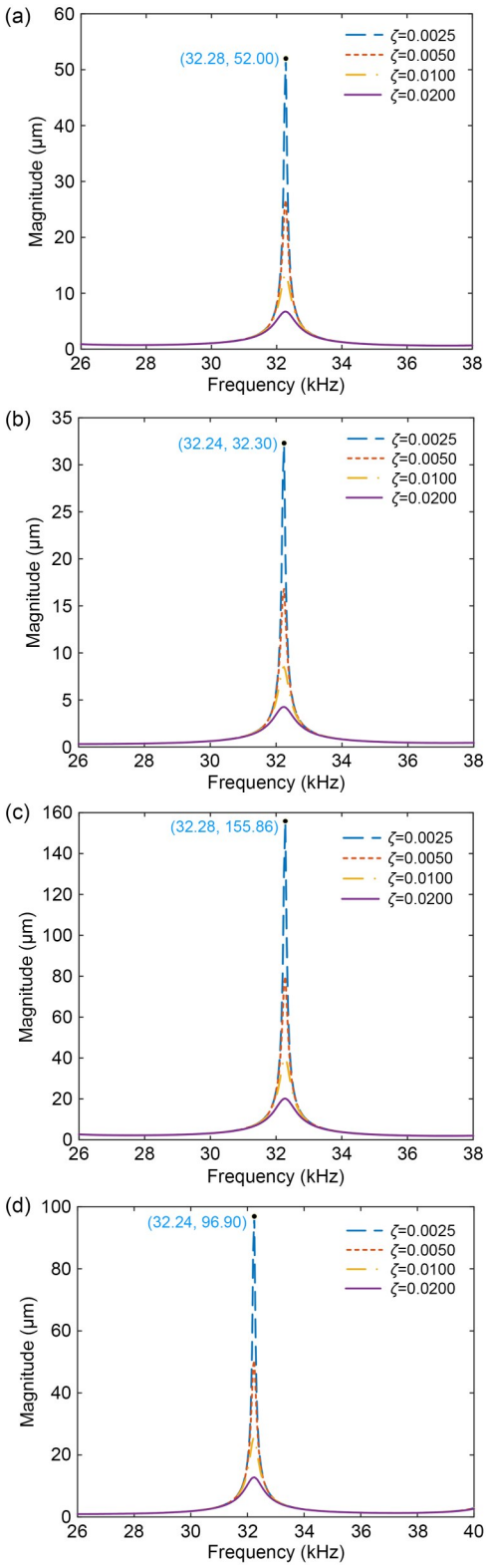


**Fig. 14 FRF simulated harmonic response of an ultrasonic transducer with different damping ratios at a given voltage of 100 V with stainless steel (a) and titanium alloy (b), and at a given voltage of 300 V with stainless steel (c) and titanium alloy (d)**

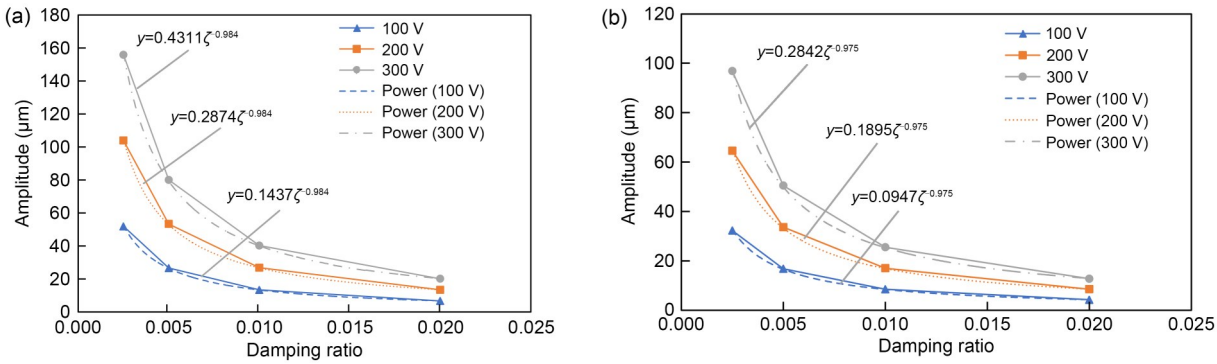


**Fig. 15 Determination of the damping ratio versus amplitude of stainless steel (a) and titanium alloy (b)**

**Table 7 Amplitude prediction according to the damping ratio**

| Material | Input voltage (V) | Amplitude (μm) | | | Error (%) |
|---|---|---|---|---|---|
| | | Simulation | Simulation$_{cal}$ | Experiment | |
| Stainless steel (SS 316L) | 100 | 6.7185 (ζ: 0.0200) | 9.2055 (ζ: 0.014600) | 9.18715 | 0.19 |
| | 200 | 13.4370 (ζ: 0.0200) | 17.4100 (ζ: 0.015440) | 17.41000 | 0.00 |
| | 300 | 20.1560 (ζ: 0.0200) | 22.0920 (ζ: 0.018250) | 22.15088 | 0.26 |
| Titanium alloy (Ti-6Al-4V) | 100 | 8.5051 (ζ: 0.0100) | 15.6690 (ζ: 0.005381) | 15.44429 | 1.45 |
| | 200 | 17.0100 (ζ: 0.0100) | 20.4890 (ζ: 0.008289) | 20.28187 | 1.02 |
| | 300 | 25.5150 (ζ: 0.0100) | 25.8070 (ζ: 0.009886) | 25.61546 | 0.74 |

Simulation$_{cal}$: simulated amplitude after calibration of the damping ratio with the experimental amplitude

amplitude was different with the experimental amplitude, except at the highest voltage, which produced a similar amplitude. Therefore, after calibration of the damping ratio with the experimental amplitude, the simulated amplitude provided a similar amplitude to the experimental amplitude, and the error was less than 1.5%.

The damping ratio significantly affects the accuracy of the predicted amplitude. Therefore, a damping ratio between 0.015 and 0.020 should be selected for stainless steel, while a damping ratio between 0.005 and 0.010 should be selected for titanium alloy. Titanium alloy has a lower Young's modulus and density than stainless steel. On the other hand, it gave a higher amplitude in the experiment. Therefore, the damping ratio for titanium alloy should be set lower than that for stainless steel.

### 6.3 UVAM outcomes

Fig. 16 compares the cutting force of CM and UVAM with different feed rates from 50 to 150 mm/min in a slot-milling operation on Al 6061 (aluminum alloy). The magnification of the cutting forces in Fig. 16 shows the similarity of the force pattern between CM and UVAM. Nevertheless, the cutting-force evidence shows that the peak-to-peak value decreased in the case of UVAM, particularly at lower feed rates such as 50 mm/min. We attribute the decline in cutting force to the axial-tool vibration effect. When the cutter end mill rotated at low feed rates, such as 50 mm/min (4.167 μm/tooth), the uncut chip thickness (4.167 μm) fell slightly lower than the critical chip thickness ($h_{min}$ ≈ 4.69 μm), such that the undeformed chip was not cut effectively. The critical chip thickness equals the coefficient ratio (0.4) multiplied by $r_{edge}$ (11.72 μm). A smearing and plowing process generally occurs on the surface when using CM because the uncut chip is not thick enough (Kurniawan et al., 2017). At a low feed rate, chip removal becomes inconsistent, as shown in Fig. 16. It is indicated by the unknown peak due to smearing and plowing. Therefore, when vibration is added, the cutting state becomes more stable and better at a low feed rate in UVAM.

In ductile machining, decreasing the feed rate also means decreasing the uncut-chip thickness. Therefore, the root mean square (RMS) load is the lowest at the lowest feed rate, such as 50 mm/min. The RMS of the cutting forces ($F_x$, $F_y$, and $F_z$) are taken between the start and end of each cut, as expressed by Eq. (14).

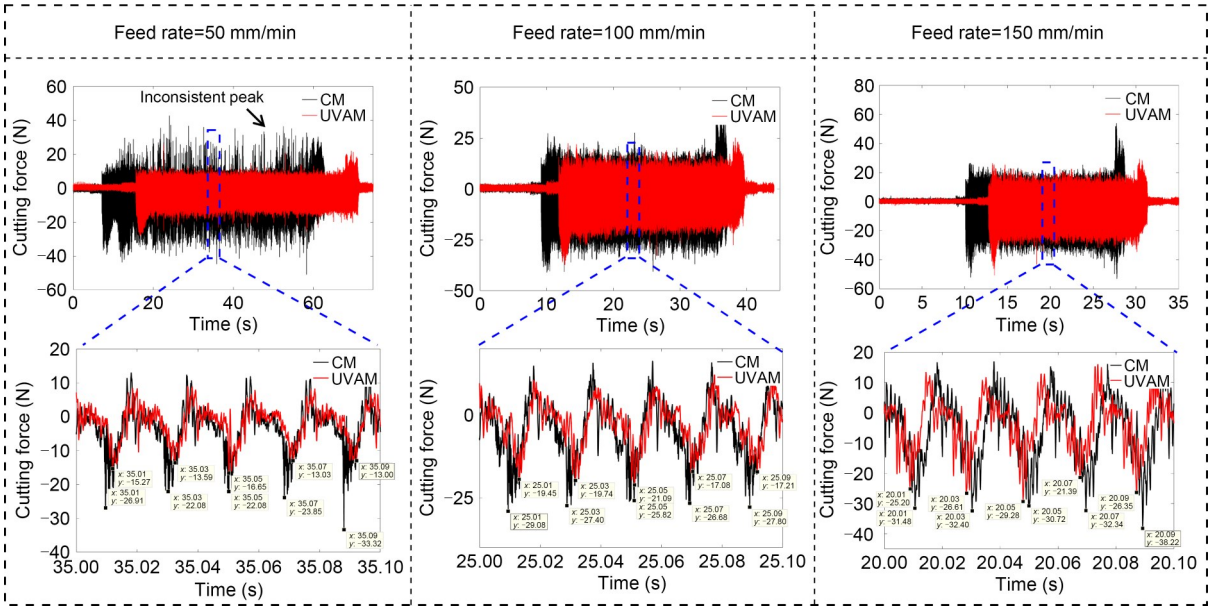


**Fig. 16 Cutting force and magnification at various feed rates. References to color refer to the online version of this figure**

$$F_{\mathrm{RMS}}=\sqrt{\frac{1}{N_{\mathrm{s}}}\left(F_i^2+F_{i+1}^2+F_{i+2}^2+\ldots+F_{N_{\mathrm{s}}}^2\right)}, \quad (14)$$

where $N_{\mathrm{s}}$ is the amount of data until end of cutting, and subscript $i$ is the force index at the beginning of cutting.

Fig. 17 demonstrates the RMS loads for both cases (CM and UVAM) for $F_x$, $F_y$, and $F_z$. The RMS load increased as the feed rate increased. The RMS instantaneous cutting force for UVAM was approximately 20%–30% lower than that for CM. We pinpointed the effects of acoustic softening (Verma et al., 2018), tool-kinematic/vibration speed (Feng et al., 2021), and intermittent cutting (Shen et al., 2012b) as reasons for the decreased cutting force in UVAM. An identical reduction of cutting force along the feed direction in UVAM when cutting ductile materials has been reported in previous studies (Shen et al., 2012b; Tao et al., 2017; Ni et al., 2018).

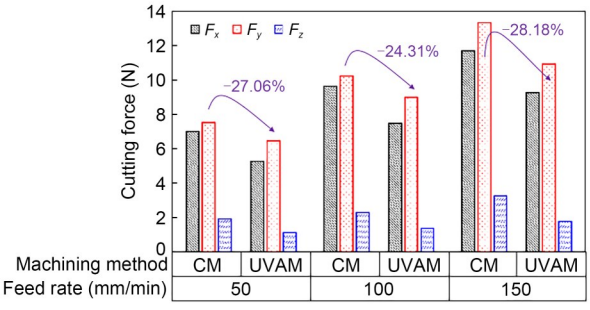


**Fig. 17 RMS force results at various feed rates**

Fig. 18 illustrates the machined surface topography for both CM and UVAM. Scratches occur because of the smearing and plowing process at a low cutting feed rate. The arithmetic average roughness $R_{\mathrm{a}}$ resulting from UVAM was lower than that produced by CM for all feed rates. The average value was taken three times using a surface-roughness tester along the feed direction. We attribute the lower $R_{\mathrm{a}}$ from UVAM to the smaller size of the pits and scratches. In addition, there were many scratches due to smearing and plastic shearing deformation resulting from CM. Chang et al. (2022) reported similar findings when comparing the surface quality between CM and UVAM. There were obvious pits on the 3D surface-topography profile for both CM and UVAM. However, the size of the pits observed for UVAM was smaller than that for CM because of the lower cutting energy applied when accidentally removing hard inclusions from the surface material. Hard inclusions are an impurity consisting of Si particles in the aluminum alloy (Al 6061) (Kurniawan and Ko, 2019), and they are typical of an Al 6061 surface (Adesola et al., 2013). In addition, we discovered vibration marks on the UVAM surface, which suggests that the oscillation tool delivers a vibration. Better material removal was obtained using UVAM, according to these results. Textured surface generation after UVAM became common findings in this field in general. A few similarities in surface topography results from UVAM along the feed direction on other ductile materials are

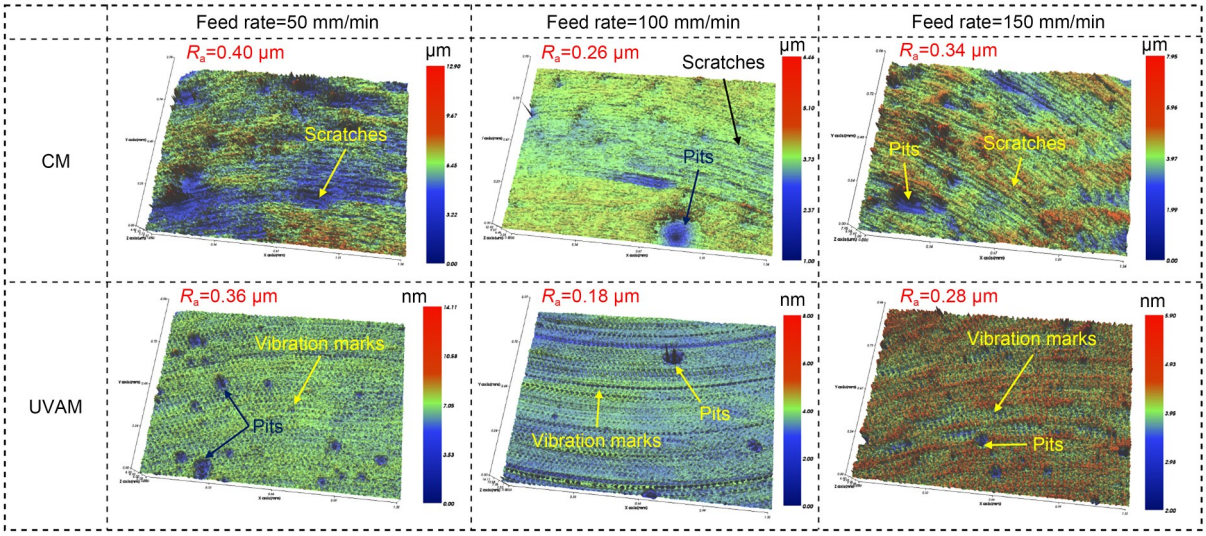


**Fig. 18 Surface topography comparison at various feed rates**

described elsewhere (Chen et al., 2019; Zhu et al., 2019; Shen et al., 2020; Lu et al., 2021).

## 7 Conclusions

We proposed an ultrasonic transducer with high frequency and amplitude. The focus of the study was on vibration characteristics, amplitude estimation, impedance-frequency prediction, and evaluation of machining performance. We assessed an electromechanical impedance model and the effect of OL and different materials. We were able to draw the following conclusions:

1. The frequency of the ultrasonic transducer depends on the preload compression stress, which remains constant when a sufficient stress of approximately 20 MPa has been obtained. Titanium alloy gives a higher resonance ultrasonic frequency (approximately 33 kHz). Stainless steel gives a lower resonance ultrasonic frequency of approximately 30 kHz. In addition, titanium alloy gives the highest amplitude of approximately 25.6 μm, using the highest input voltage.

2. The electromechanical impedance simulation predicted resonance frequency with less than 3% error, and is thus useful for predicting the resonance ultrasonic frequency of ultrasonic transducers in the absence of a cutting load. In addition, the OL affects the natural oscillation frequency. When the OL increases, the resonance frequency decreases, indicating a larger acoustic half-wavelength.

3. Harmonic simulation can be used to predict resonance amplitude. However, it is necessary to determine the damping ratio by calibration in order to estimate resonance amplitude precisely. The damping ratio of stainless steel was 0.015–0.020; the damping ratio of titanium alloy was 0.005–0.010. The error for amplitude prediction using harmonic simulation was less than 1.5%.

4. The feasibility study of the ultrasonic transducer for UVAM shows that the cutting load and surface topography profile are better than those for CM with various feed rates. The RMS cutting force is about 20%–30% lower in UVAM. The cutting state becomes more stable at a low feed rate when UVAM is induced. In addition, smaller pits and scratches are produced by UVAM. These results prove that the ultrasonic transducer can be used in industrial applications for non-conventional milling or drilling.

## Acknowledgments

This work is supported by Korea Electrotechnology Research Institute (KERI) Primary Research Program through the National Research Council of Science & Technology (NST) funded by the Ministry of Science and ICT (MSIT) in 2023 (No. 23A01021) and the National Research Foundation of Korea (NRF) grant funded by the Korean Government (MSIT) (No. RS-2023-00278890).

## Author contributions

Rendi KURNIAWAN: writing–original draft, formal analysis, software, conceptualization, and methodology. Moran XU and Shuo CHEN: resources, visualization, and investigation. Jielin CHEN, Hanwei TENG, and Saood ALI: software and

validation. Yein KWAK and Min Ki CHOO: project administration. Pil Wan HAN: supervision and funding acquisition. Gi Soo KIM: conceptualization and resources. Tae Jo KO: funding acquisition, supervision, and writing–review & editing.

## Conflict of interest

Rendi KURNIAWAN, Moran XU, Min Ki CHOO, Shuo CHEN, Yein KWAK, Jielin CHEN, Saood ALI, Hanwei TENG, Pil Wan HAN, Gi Soo KIM, and Tae Jo KO declare that they have no conflict of interest.

## References

Adesola AO, Odeshi AG, Lanke UD, 2013. The effects of aging treatment and strain rates on damage evolution in AA 6061 aluminum alloy in compression. *Materials & Design*, 45:212-221. https://doi.org/10.1016/j.matdes.2012.08.021

Al Ahmad M, Plana R, 2009. Vertical displacement detection of an aluminum nitride piezoelectric thin film using capacitance measurements. *International Journal of Microwave and Wireless Technologies*, 1(1):5-9. https://doi.org/10.1017/s1759078709000026

Amini S, Soleimanimehr H, Nategh MJ, et al., 2008. FEM analysis of ultrasonic-vibration-assisted turning and the vibratory tool. *Journal of Materials Processing Technology*, 201(1-3):43-47. https://doi.org/10.1016/j.jmatprotec.2007.11.271

Babitsky VI, Astashev VK, Kalashnikov AN, 2004. Autoresonant control of nonlinear mode in ultrasonic transducer for machining applications. *Ultrasonics*, 42(1-9):29-35. https://doi.org/10.1016/j.ultras.2004.01.004

Bie WB, Zhao B, Zhao CY, et al., 2021. System design and experimental research on the tangential ultrasonic vibration-assisted grinding gear. *The International Journal of Advanced Manufacturing Technology*, 116:597-610. https://doi.org/10.1007/s00170-021-07459-8

Boccaccini AR, 1997. Machinability and brittleness of glass-ceramics. *Journal of Materials Processing Technology*, 65(1-3):302-304. https://doi.org/10.1016/S0924-0136(96)02275-3

Bybi A, Mouhat O, Garoum M, et al., 2019. One-dimensional equivalent circuit for ultrasonic transducer arrays. *Applied Acoustics*, 156:246-257. https://doi.org/10.1016/j.apacoust.2019.07.011

Chang BQ, Yi ZX, Cao XB, et al., 2022. Surface feature and material removal in ultrasonic vibration-assisted slot-milling of Ti–6Al–4 V titanium alloy. *The International Journal of Advanced Manufacturing Technology*, 122:2235-2251. https://doi.org/10.1007/s00170-022-09970-y

Chen WQ, Huo DH, Shi YL, et al., 2018. State-of-the-art review on vibration-assisted milling: principle, system design, and application. *The International Journal of Advanced Manufacturing Technology*, 97(5-8):2033-2049. https://doi.org/10.1007/s00170-018-2073-z

Chen WQ, Zheng L, Xie WK, et al., 2019. Modelling and experimental investigation on textured surface generation in vibration-assisted micro-milling. *Journal of Materials Processing Technology*, 266:339-350. https://doi.org/10.1016/j.jmatprotec.2018.11.011

Chen YR, Su HH, He JY, et al., 2021. The effect of torsional vibration in longitudinal-torsional coupled ultrasonic vibration-assisted grinding of silicon carbide ceramics. *Materials (Basel)*, 14(3):688. https://doi.org/10.3390/ma14030688

Chen ZP, Zhao XH, Chen SX, et al., 2022. Analysis of ultrasonic machining characteristics under dynamic load. *Sensors (Basel)*, 22(21):8576. https://doi.org/10.3390/s22218576

Choudhury IA, El-Baradie MA, 1998. Machinability of nickel-base super alloys: a general review. *Journal of Materials Processing Technology*, 77(1-3):278-284. https://doi.org/10.1016/S0924-0136(97)00429-9

Cornogolub A, Cottinet PJ, Petit L, 2014. Analytical modeling of curved piezoelectric, Langevin-type, vibrating transducers using transfer matrices. *Sensors and Actuators A: Physical*, 214:120-133. https://doi.org/10.1016/j.sna.2014.04.003

DeAngelis DA, Schulze GW, 2016. Performance of PZT8 versus PZT4 piezoceramic materials in ultrasonic transducers. *Physics Procedia*, 87:85-92. https://doi.org/10.1016/j.phpro.2016.12.014

DeAngelis DA, Schulze GW, Wong KS, 2015. Optimizing piezoelectric stack preload bolts in ultrasonic transducers. *Physics Procedia*, 63:11-20. https://doi.org/10.1016/j.phpro.2015.03.003

Feng YX, Hsu FC, Lu YT, et al., 2021. Force prediction in ultrasonic vibration-assisted milling. *Machining Science and Technology*, 25(2):307-330. https://doi.org/10.1080/10910344.2020.1815048

Gao J, Altintas Y, 2019. Development of a three-degree-of-freedom ultrasonic vibration tool holder for milling and drilling. *IEEE/ASME Transactions on Mechatronics*, 24(3):1238-1247. https://doi.org/10.1109/tmech.2019.2906904

Geng DX, Zhang DY, Xu YG, et al., 2014. Comparison of drill wear mechanism between rotary ultrasonic elliptical machining and conventional drilling of CFRP. *Journal of Reinforced Plastics and Composites*, 33(9):797-809. https://doi.org/10.1177/0731684413518619

Geng DX, Zhang DY, Xu YG, et al., 2015. Rotary ultrasonic elliptical machining for side milling of CFRP: tool performance and surface integrity. *Ultrasonics*, 59:128-137. https://doi.org/10.1016/j.ultras.2015.02.006

Han X, Zhang DY, 2020. Effects of separating characteristics in ultrasonic elliptical vibration-assisted milling on cutting force, chip, and surface morphologies. *The International Journal of Advanced Manufacturing Technology*, 108:3075-3084. https://doi.org/10.1007/s00170-020-05463-y

Jagadish, Ray A, 2018. Design and performance analysis of ultrasonic horn with a longitudinally changing rectangular cross section for USM using finite element analysis. *Journal of the Brazilian Society of Mechanical Sciences and Engineering*, 40(7):359. https://doi.org/10.1007/s40430-018-1281-7

Jallageas J, K'nevez JY, Chérif M, et al., 2013. Modeling and optimization of vibration-assisted drilling on positive feed drilling unit. *The International Journal of Advanced Manufacturing Technology*, 67:1205-1216.

https://doi.org/10.1007/s00170-012-4559-4

Kandi R, Sahoo SK, Sahoo AK, 2020. Ultrasonic vibration-assisted turning of titanium alloy Ti–6Al–4V: numerical and experimental investigations. *Journal of the Brazilian Society of Mechanical Sciences and Engineering*, 42(8):399. https://doi.org/10.1007/s40430-020-02481-5

Kremer D, Saleh SM, Ghabrial SR, et al., 1981. The state of the art of ultrasonic machining. *CIRP Annals*, 30(1):107-110. https://doi.org/10.1016/s0007-8506(07)60905-6

Kumar S, Wu CS, Padhy GK, et al., 2017. Application of ultrasonic vibrations in welding and metal processing: a status review. *Journal of Manufacturing Processes*, 26:295-322. https://doi.org/10.1016/j.jmapro.2017.02.027

Kurniawan R, Ko TJ, 2019. Surface topography analysis in three-dimensional elliptical vibration texturing (3D-EVT). *The International Journal of Advanced Manufacturing Technology*, 102:1601-1621. https://doi.org/10.1007/s00170-018-03253-1

Kurniawan R, Kiswanto G, Ko TJ, 2017. Surface roughness of two-frequency elliptical vibration texturing (TFEVT) method for micro-dimple pattern process. *International Journal of Machine Tools and Manufacture*, 116:77-95. https://doi.org/10.1016/j.ijmachtools.2016.12.011

Kurniawan R, Ali S, Park KM, et al., 2019. Development of a three-dimensional ultrasonic elliptical vibration transducer (3D-UEVT) based on sandwiched piezoelectric actuator for micro-grooving. *International Journal of Precision Engineering and Manufacturing*, 20(7):1229-1240. https://doi.org/10.1007/s12541-019-00126-9

Kurniawan R, Ko TJ, Kumaran ST, et al., 2021. 3-DOF ultrasonic elliptical vibration tool holder based on coupled resonance modes for manufacturing micro-groove. *Precision Engineering*, 67:212-231. https://doi.org/10.1016/j.precisioneng.2020.10.002

Kuruc M, 2020. Machining of composite materials by ultrasonic assistance. *Advances in Science and Technology Research Journal*, 14(2):140-144. https://doi.org/10.12913/22998624/118943

Li C, Zhang FH, Meng BB, et al., 2017. Material removal mechanism and grinding force modelling of ultrasonic vibration assisted grinding for SiC ceramics. *Ceramics International*, 43(3):2981-2993. https://doi.org/10.1016/j.ceramint.2016.11.066

Li G, Qu JS, Xu L, et al., 2022. Study on multi-frequency characteristics of a longitudinal ultrasonic transducer with stepped horn. *Ultrasonics*, 121:106683. https://doi.org/10.1016/j.ultras.2022.106683

Li HB, Chen T, Song H, et al., 2021. Design and experimental study of longitudinal-torsional ultrasonic transducer with helical slots considering the stiffness variation. *The International Journal of Advanced Manufacturing Technology*, 114:3093-3107. https://doi.org/10.1007/s00170-021-06802-3

Lin SY, Guo H, Xu J, 2018. Actively adjustable step-type ultrasonic horns in longitudinal vibration. *Journal of Sound and Vibration*, 419:367-379. https://doi.org/10.1016/j.jsv.2018.01.033

Liu S, Shan XB, Cao W, et al., 2017. A longitudinal-torsional composite ultrasonic vibrator with thread grooves. *Ceramics International*, 43:S214-S220. https://doi.org/10.1016/j.ceramint.2017.05.305

Liu YH, Zhang DY, Geng DX, et al., 2023. Ironing effect on surface integrity and fatigue behavior during ultrasonic peening drilling of Ti-6Al-4V. *Chinese Journal of Aeronautics*, 36(5):486-498. https://doi.org/10.1016/j.cja.2022.12.009

Lu H, Zhu LD, Yang ZC, et al., 2021. Research on the generation mechanism and interference of surface texture in ultrasonic vibration assisted milling. *International Journal of Mechanical Sciences*, 208:106681. https://doi.org/10.1016/j.ijmecsci.2021.106681

Marcel K, Marek Z, Jozef P, 2014. Investigation of ultrasonic assisted milling of aluminum alloy AlMg4.5Mn. *Procedia Engineering*, 69:1048-1053. https://doi.org/10.1016/j.proeng.2014.03.089

McBrearty M, Kim LH, Bilgutay NM, 1988. Analysis of impedance loading in ultrasonic transducer systems. IEEE 1988 Ultrasonics Symposium Proceedings, p.497-502. https://doi.org/10.1109/ultsym.1988.49427

Milewski A, Kluk P, Kardyś W, et al., 2015. Modelling and designing of ultrasonic welding systems. *Archives of Acoustics*, 40(1):93-99. https://doi.org/10.1515/aoa-2015-0011

Namlu RH, Yılmaz OD, Lotfisadigh B, et al., 2022. An experimental study on surface quality of Al6061-T6 in ultrasonic vibration-assisted milling with minimum quantity lubrication. *Procedia CIRP*, 108:311-316. https://doi.org/10.1016/j.procir.2022.04.071

Ni CB, Zhu LD, Liu CF, et al., 2018. Analytical modeling of tool-workpiece contact rate and experimental study in ultrasonic vibration-assisted milling of Ti−6Al−4V. *International Journal of Mechanical Sciences*, 142-143:97-111. https://doi.org/10.1016/j.ijmecsci.2018.04.037

Noda NA, Hu KJ, Sano Y, et al., 2017. Accuracy of disk method to predict roll residual stress by measuring the sliced disk stress. *ISIJ International*, 57(8):1433-1441. https://doi.org/10.2355/isijinternational.ISIJINT-2016-653

Ostasevicius V, Gaidys R, Dauksevicius R, et al., 2013. Study of vibration milling for improving surface finish of difficult-to-cut materials. *Strojniški Vestnik–Journal of Mechanical Engineering*, 59(6):351-357. https://doi.org/10.5545/sv-jme.2012.856

Othmani C, Zhang H, Lü CF, 2020. Effects of initial stresses on guided wave propagation in multilayered PZT-4/PZT-5A composites: a polynomial expansion approach. *Applied Mathematical Modelling*, 78:148-168. https://doi.org/10.1016/j.apm.2019.10.017

Pang Y, Feng PF, Zhang JF, et al., 2020. Frequency coupling design of ultrasonic horn with spiral slots and performance analysis of longitudinal-torsional machining characteristics. *The International Journal of Advanced Manufacturing Technology*, 106:4093-4103. https://doi.org/10.1007/s00170-019-04898-2

Pang Y, Feng PF, Wang JJ, et al., 2021. Performance analysis of the longitudinal-torsional ultrasonic milling of Ti-6Al-4V. *The International Journal of Advanced Manufacturing Technology*, 113:1255-1266. https://doi.org/10.1007/s00170-021-06682-7

Patel LK, Singh AK, Sharma V, et al., 2021. Analysis of a hybrid ultrasonic horn profile using finite element analysis. *Materials Today: Proceedings*, 41:772-779. https://doi.org/10.1016/j.matpr.2020.08.465

Pérez-Sánchez A, Segura JA, Rubio-Gonzalez C, et al., 2020. Numerical design and analysis of a Langevin power ultrasonic transducer for acoustic cavitation generation. *Sensors and Actuators A: Physical*, 311:112035. https://doi.org/10.1016/j.sna.2020.112035

Shamoto E, Suzuki N, Tsuchiya E, et al., 2005. Development of 3 DOF ultrasonic vibration tool for elliptical vibration cutting of sculptured surfaces. *CIRP Annals*, 54(1):321-324. https://doi.org/10.1016/s0007-8506(07)60113-9

Shen XH, Zhang JH, Xing DX, et al., 2012a. A study of surface roughness variation in ultrasonic vibration-assisted milling. *The International Journal of Advanced Manufacturing Technology*, 58:553-561. https://doi.org/10.1007/s00170-011-3399-y

Shen XH, Zhang JH, Li H, et al., 2012b. Ultrasonic vibration-assisted milling of aluminum alloy. *The International Journal of Advanced Manufacturing Technology*, 63:41-49. https://doi.org/10.1007/s00170-011-3882-5

Shen XH, Shi YL, Zhang JH, et al., 2020. Effect of process parameters on micro-textured surface generation in feed direction vibration assisted milling. *International Journal of Mechanical Sciences*, 167:105267. https://doi.org/10.1016/j.ijmecsci.2019.105267

Tao GC, Ma C, Shen XH, et al., 2017. Experimental and modeling study on cutting forces of feed direction ultrasonic vibration-assisted milling. *The International Journal of Advanced Manufacturing Technology*, 90:709-715. https://doi.org/10.1007/s00170-016-9421-7

Thoe TB, Aspinwall DK, Wise MLH, 1998. Review on ultrasonic machining. *International Journal of Machine Tools and Manufacture*, 38(4):239-255. https://doi.org/10.1016/S0890-6955(97)00036-9

van Kervel SJH, Thijssen JM, 1983. A calculation scheme for the optimum design of ultrasonic transducers. *Ultrasonics*, 21(3):134-140. https://doi.org/10.1016/0041-624X(83)90033-1

Verma GC, Pandey PM, Dixit US, 2018. Modeling of static machining force in axial ultrasonic-vibration assisted milling considering acoustic softening. *International Journal of Mechanical Sciences*, 136:1-16. https://doi.org/10.1016/j.ijmecsci.2017.11.048

Voronina S, Babitsky V, 2008. Autoresonant control strategies of loaded ultrasonic transducer for machining applications. *Journal of Sound and Vibration*, 313(3-5):395-417. https://doi.org/10.1016/j.jsv.2007.12.014

Wang JJ, Feng PF, Zhang JF, et al., 2018. Reducing cutting force in rotary ultrasonic drilling of ceramic matrix composites with longitudinal-torsional coupled vibration. *Manufacturing Letters*, 18:1-5. https://doi.org/10.1016/j.mfglet.2018.08.002

Wang L, Hofmann V, Bai FS, et al., 2018. Modeling of coupled longitudinal and bending vibrations in a sandwich type piezoelectric transducer utilizing the transfer matrix method. *Mechanical Systems and Signal Processing*, 108:216-237. https://doi.org/10.1016/j.ymssp.2018.02.022

Wang SH, Tsai MC, 2011. Dynamic modeling of thickness-mode piezoelectric transducer using the block diagram approach. *Ultrasonics*, 51(5):617-624. https://doi.org/10.1016/j.ultras.2011.01.002

Wang Y, Lin B, Wang SL, et al., 2014. Study on the system matching of ultrasonic vibration assisted grinding for hard and brittle materials processing. *International Journal of Machine Tools and Manufacture*, 77:66-73. https://doi.org/10.1016/j.ijmachtools.2013.11.003

Wu CJ, Chen SJ, Cheng K, et al., 2019. Innovative design and analysis of a longitudinal-torsional transducer with the shared node plane applied for ultrasonic assisted milling. *Proceedings of the Institution of Mechanical Engineers, Part C: Journal of Mechanical Engineering Science*, 233(12):4128-4139. https://doi.org/10.1177/0954406218797962

Xia Y, Wan Y, Luo XC, et al., 2020. Chatter suppression in large overhang face milling using a toolholder with high dynamic performance. *The International Journal of Advanced Manufacturing Technology*, 108:1713-1724. https://doi.org/10.1007/s00170-020-05515-3

Yang Y, Wei XY, Zhang L, et al., 2017. The effect of electrical impedance matching on the electromechanical characteristics of sandwiched piezoelectric ultrasonic transducers. *Sensors (Basel)*, 17(12):2832. https://doi.org/10.3390/s17122832

Zhang CL, Cong WL, Feng PF, et al., 2014. Rotary ultrasonic machining of optical K9 glass using compressed air as coolant: a feasibility study. *Proceedings of the Institution of Mechanical Engineers, Part B: Journal of Engineering Manufacture*, 228(4):504-514. https://doi.org/10.1177/0954405413506195

Zhang JG, Long ZL, Ma WJ, et al., 2019. Electromechanical dynamics model of ultrasonic transducer in ultrasonic machining based on equivalent circuit approach. *Sensors*, 19(6):1405. https://doi.org/10.3390/s19061405

Zhang M, Zhang D, Geng D, et al., 2020. Surface and subsurface analysis of rotary ultrasonic elliptical end milling of Ti-6Al-4V. *Materials & Design*, 191:108658. https://doi.org/10.1016/j.matdes.2020.108658

Zhang Q, Shi SJ, Chen WS, 2015. An electromechanical coupling model of a longitudinal vibration type piezoelectric ultrasonic transducer. *Ceramics International*, 41(Supplement 1):S638-S644. https://doi.org/10.1016/j.ceramint.2015.03.200

Zhao B, Bie WB, Wang XB, et al., 2019. Design and experimental investigation on longitudinal-torsional composite horn considering the incident angle of ultrasonic wave. *The International Journal of Advanced Manufacturing Technology*, 105:325-341. https://doi.org/10.1007/s00170-019-04220-0

Zheng L, Chen WQ, Huo DH, 2020. Review of vibration devices for vibration-assisted machining. *The International Journal of Advanced Manufacturing Technology*, 108:1631-1651. https://doi.org/10.1007/s00170-020-05483-8

Zhu LD, Ni CB, Yang ZC, et al., 2019. Investigations of micro-textured surface generation mechanism and tribological properties in ultrasonic vibration-assisted milling of Ti–6Al–4V. *Precision Engineering*, 57:229-243. https://doi.org/10.1016/j.precisioneng.2019.04.010

## Electronic supplementary materials

Section S1, Table S1